Laboratory simulation of impacts upon aluminium foils of the Stardust spacecraft: Calibration of dust particle size from comet Wild2.

A.T. Kearsley [1], M.J. Burchell[2], F. Hörz[3], M.J. Cole[2] and C.S. Schwandt[3]

[1] Impact and Astromaterials Research Centre, Department of Mineralogy, The Natural History Museum London, SW7 5BD antk@nhm.ac.uk;
[2] Centre for Astrophysics and Planetary Sciences, School of Physical Science, University of Kent, Canterbury, Kent CT2 7NH, UK;
[3] NASA Johnson Space Center, Houston, TX 77058, USA.

Abstract - Metallic aluminium alloy foils exposed on the forward, comet-facing surface of the aerogel tray on the Stardust spacecraft are likely to have been impacted by the same cometary particle population as the dedicated impact sensors and the aerogel collector. The ability of soft aluminium alloy to record hypervelocity impacts as bowl-shaped craters offers an opportunistic substrate for recognition of impacts by particles of a wide potential size range. In contrast to impact surveys conducted on samples from low Earth orbit, the simple encounter geometry for Stardust and Wild 2, with a known and constant spacecraft-particle relative velocity and effective surface-perpendicular impact trajectories, permits closely comparable simulation in laboratory experiments. For a detailed calibration programme we have selected a suite of spherical glass projectiles of uniform density and hardness characteristics, with well-documented particle size range from 10 microns to nearly 100 microns. Light gas gun buckshot firings of these particles at approximately 6km s^{-1} onto samples of the same foil as employed on Stardust have yielded large numbers of craters. Scanning electron microscopy of both projectiles and impact features has allowed construction of a calibration plot, showing a linear relationship between impacting particle size and impact crater diameter. The close match between our experimental conditions and the Stardust mission encounter parameters should provide another opportunity to measure particle size distributions and fluxes close to the nucleus of Wild 2, independent of the active impact detector instruments aboard the Stardust spacecraft.

INTRODUCTION

The Stardust mission has a primary objective of the collection of cometary dust particles from comet Wild 2, and their return to Earth (Brownlee *et al*., 2003). The time-line, geometry and velocity for the encounter with Wild 2 are described by Brownlee *et al*., 2003 and the aerogel collection system is described by Tsou *et al*., 2003. Real-time sensors aboard the spacecraft detected a large number of particle impacts during the 264 seconds before and 922 seconds after closest approach to the comet nucleus (Tuzzolino *et al*., 2004). Data from the bumpershield impact detection sensors suggests that 2800±500 particles with size greater than 15 µm have been implanted within exposed silica aerogel blocks (Tuzzolino et al., 2004) which will form the main focus of post-flight investigation. However, it should be noted that the two real-time detection systems on board the spacecraft returned impact data (Kissel *et al*., 2003, Tuzzolino *et al*., 2004), with different sensitivities in terms of momentum threshold (i.e. the range of mass and velocity product), and there are apparent discrepancies between their impact count rates (Tsou *et al*., 2004). The impact

ionization system (Kissel et al., 2003) indicated a significantly lower flux than the more widely reported bumpershield data. Laboratory experiments utilising monomineralic and powdered meteorite projectiles of greater than 20 microns diameter have shown that remnants of these grains can be recognised in impact tracks within aerogel, although there is often evidence of fragmentation during emplacement (Graham et al., 2005), making determination of original particle size very difficult. The potential extent of this problem is shown by observations of aerogel exposed on the Mir station, where the measured size of projectile residue had no systematic relationship with the size of penetration tracks (Hörz et al., 2000). It has not yet been convincingly demonstrated that much smaller silicate particles (e.g. 1 micron diameter) will leave recognisable traces in aerogel. Evidence from interplanetary dust detectors (e.g. Grün et al., 1992; Grün et al., 1995) and from spacecraft materials returned from low Earth orbit (e.g. Moussi *et al*., 2005) suggests that there are abundant micrometeoroids of micron scale, although the relative contribution from asteroid and comet sources has not yet been firmly established. Although not widely realised, another component of the Stardust spacecraft may yield valuable information as to the size distribution of particles encountered. In addition to the 1039 cm^2 area of aerogel on the comet collection face, 153 cm^2 of aluminium foil (Figure 1) was also exposed to impact (Tsou et al., 2003). It is likely that these foils have preserved a record of impacts from sub-micron scale upwards.

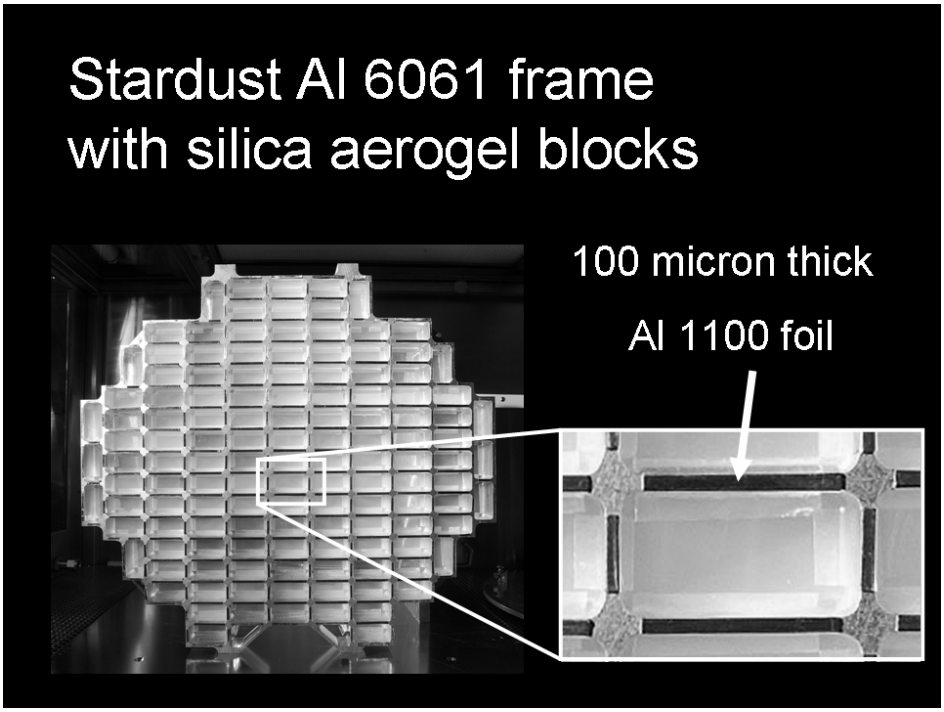

Figure 1. The Stardust aerogel collector aluminium frame, with an enlarged detail of four foil sheets (reflective, appearing dark) around an aerogel block. Image courtesy of NASA/JPL-Caltech.

Many spacecraft surfaces exposed to space in low Earth orbit (LEO) have been examined for signs of impact damage (e.g. Warren et al., 1989; Humes, 1991; See et al., 1994, Zolensky et al. 1994; Love et al., 1995; Bernhard and Hörz, 1995; Graham et al., 2001, Moussi et al., 2005). Metal surfaces present a relatively hard and dense substrate, and may therefore result in high levels of modification to the impacting

particle (Bernhard et al., 1994a; Graham et al., 2001) during the creation of a distinctive bowl-shaped crater. Aluminium alloys are the metals employed most extensively (Dunn, 1997), usually containing Mg, Mn, Fe and Cu in concentrations of a few parts per thousand to a few percent (Davis, 1998), often segregated heterogeneously on a scale of microns (e.g. Figure 4). Successful laboratory simulation of hypervelocity impact features on aluminium foils was reported by Hörz et al., 1993. Where recognition of particle origins is an important goal for an impact survey (e.g. Kearsley et al., 2005), confusion of the substrate composition with that of impacting space debris may be a problem, unless a substantial amount of residue is present (Graham et al., 2004). Fortunately, micrometeoroid remains are easily recognised on aluminium surfaces, where their distinctive mafic silicate and sulphide residues stand out (Bernhard et al., 1994a, 1994b; Brownlee et al., 1994). For surfaces that have been returned from LEO, difficulties attend interpretation of the mass of individual impacting particles, due to unconstrained variables, i.e. the crater characteristics reflect their mass and velocity, both unknown quantities that have no simple and unambiguous individual proxies. Surveys of spacecraft impact damage (e.g. Moussi et al., 2005) derive flux models detailing numbers of specific particle size, but need to rely upon assumptions of a mean velocity as well as density for micrometeoroids, which cannot fully reflect the diverse range of natural particle populations. The apparently circular outline of most impact craters may also poorly reflect the diversity of incidence angles and therefore can mask a range of effective impact velocities. Most laboratory simulations of impacts upon ductile substrates have employed a target-perpendicular shot trajectory and relatively well-constrained particle diameters, hardness, density, mass and velocity. Relatively few experiments (e.g. Christiansen et al., 1993; Burchell and MacKay, 1998) have looked at oblique incidence impacts or impacts from notably non spherical projectiles. There are thus difficulties in making direct comparison between laboratory experiments and the complex situation in LEO (Love et al. 1995). In addition, although many LEO impact features do record micrometeoroid impacts (c. 50% of the 75% of features determined, Kearsley et al. 2005) it is not possible to distinguish cometary, asteroidal and interstellar origins.

In the case of the Stardust encounter, the on-board impact sensors have demonstrated that the vast majority of the impacting particle collection on the front face of the spacecraft was acquired during the few minutes around closest approach to the nucleus of comet Wild 2 (Tuzzolino et al., 2004), with 2300±400 particles of greater than 15μm diameter captured by the aerogel. Later bursts of activity, mostly from smaller particles, were also recorded some 620-720 seconds after closest encounter with perhaps 500±200 being captured in the aerogel. Together these collections may thus be taken as a true reflection of a cometary source. The dominant component of the relative impacting velocity particle is believed to be that of the spacecraft relative to the nucleus (6.1 kms^{-1}), resulting in impacts at a known velocity at near surface-perpendicular incidence. Thus the important attributes of the Stardust mission particle to foil encounter fall neatly within the capabilities of laboratory experiments.

In addition to documenting the relationship between particle size and the diameter of the resulting crater, the theme of this paper, we have also investigated effects of particle composition, density, and hardness for a range of known projectile materials. The role of such particle properties in influencing crater morphology, and their recognition from impact residues is to be covered in a future paper. In this paper

we concentrate upon determination of impacting particle diameter from the size of impact feature.

IMAGERY AND MEASUREMENT OF PROJECTILE AND IMPACT FEATURE DIMENSIONS

All of the imagery and measurement reported in this paper was performed on a JEOL 5900 LV scanning electron microscope (SEM) in the Electron Microscopy and Mineral Analysis division of the Department of Mineralogy at the Natural History Museum, London. All images were taken using 20kV accelerating voltage at high vacuum, with backscattered electron images (BEI) and secondary electron images (SEI) of magnifications between x100 and x500 collected using an Oxford Instruments INCA X-ray energy dispersive microanalyser, running version 15 software. Entire target foils were documented by automated image montage creation (Figure 2), with storage of individual image frames for later examination at high resolution, and subsequent measurement of features using the digital callipers in the INCA software. Image size calibration was performed by collection of images from features on a Richardson high magnification test slide (model 80302, serial 10461), at the same magnifications and working distance as were employed for projectile and crater imagery, yielding an excellent linear fit across a wide size range between the published size of features on the calibration slide and the figures derived from the digital calliper measurements (Figure 3). Error on linear dimension measurements was determined as a standard deviation of less than ± 1% in all calibration images.

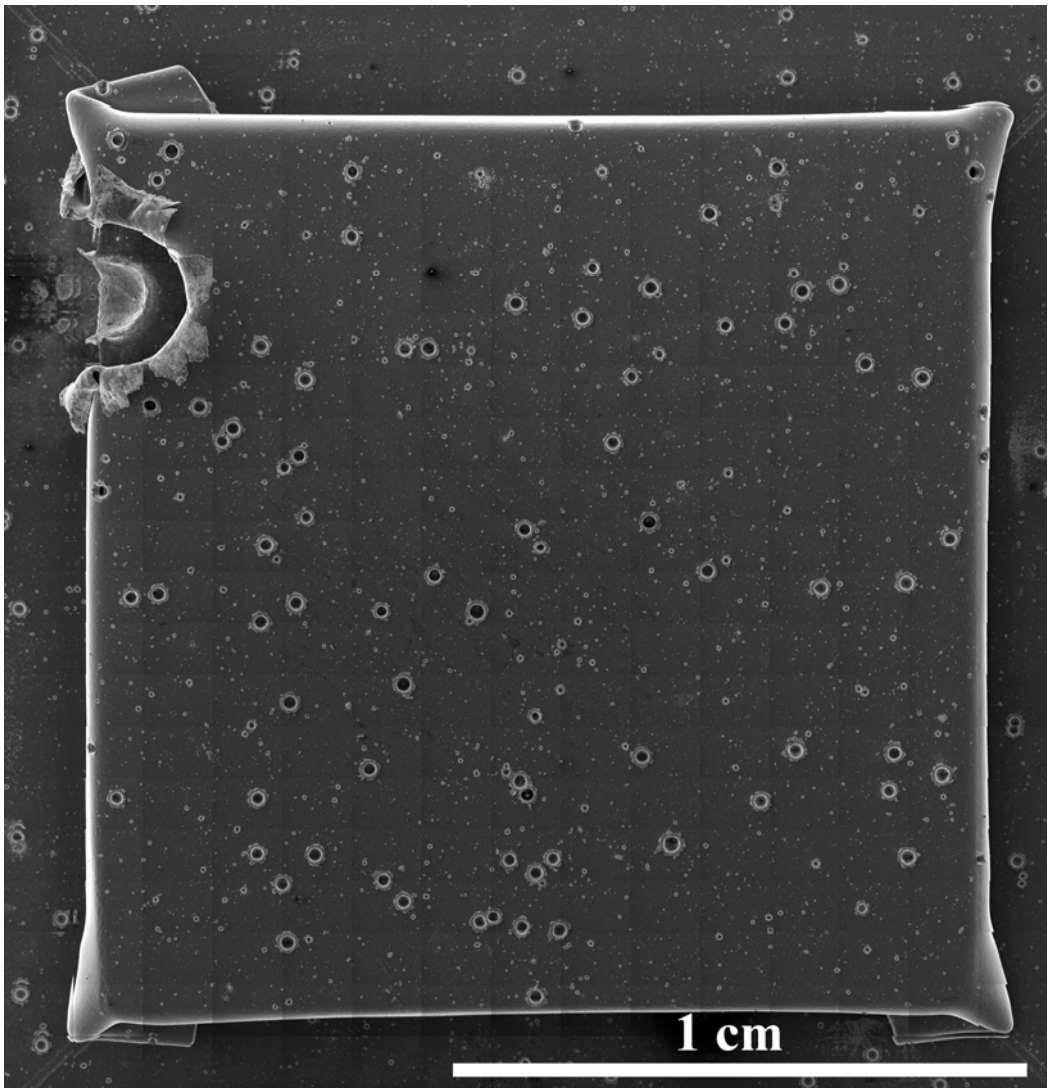

Figure 2. Montage of secondary electron images, showing numerous impacts by soda lime glass spheres, of 62 microns diameter.

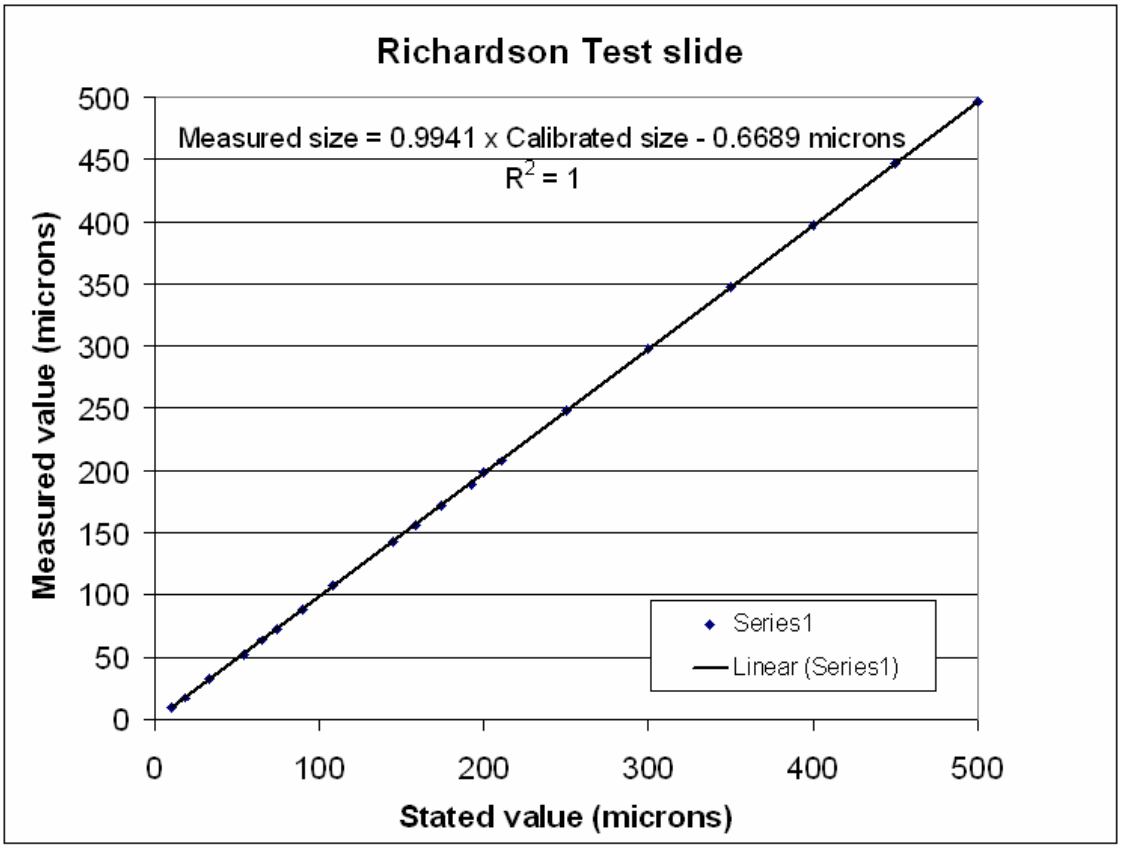

Figure 3. Plot of SEM digital caliper measurements on Richardson test slide features (Y-axis) against certified values (X-axis). Note excellent linear correlation within 1% of certified values.

IMPACT MATERIALS AND TECHNIQUES

The Target

In all shots the targets were samples of the same metal alloy foil as employed on Stardust (100 micron thickness Al 1100). The surface morphology and composition of the foil was examined by backscattered electron images of a small (c. 1cm^2) sub-sample, revealing a relatively smooth surface showing subtle linear surface striations due to the rolling fabrication process for the foil, weak electron channelling contrast delimiting metal domain structure, and bright inclusions of iron-rich phases within the alloy (Figure 4).

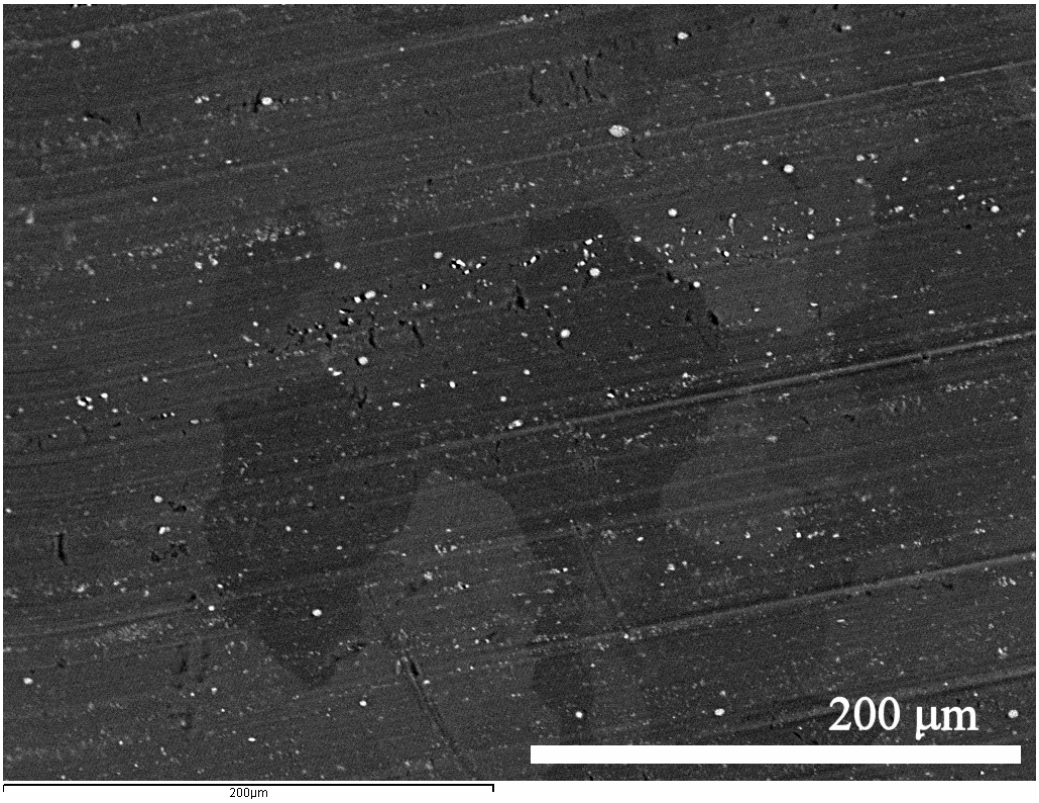

Figure 4. Backscattered electron image of a piece of the Stardust Al 1100 foil, showing linear surface striations, channelling contrast from discrete metal grains (variations in background grey-tone), and iron-rich alloy inclusions (bright areas).

Projectiles

For our extensive shot programme, projectiles were selected to evaluate the influence of a range of variables, including size, shape, density, hardness and chemical composition. The resulting impact craters have been examined to provide information upon the relationship between projectile diameter and crater diameter, deviation from circular shape as a function of projectile shape, the location of projectile residue, the modification of projectile composition, and the recognition of specific minerals likely to occur within cometary dust samples.

However, in this paper we concentrate upon the results from ten shots that utilised projectiles of a single composition (soda-lime glass), and hence similar density and hardness. To minimise dispersion of crater dimensions as a result of complex impactor morphology, we used spherical projectiles, of well-constrained size distribution. The shots at Kent and NASA each included several examples of the same projectile size for consistency checks between laboratories, and several distinct sizes to widen the calibration range. The soda lime glass beads were supplied by White House Scientific (see http://www.whitehousescientific.com/), sieved to a certified size distribution, with the error bars given in table 1 corresponding to the $\pm 1\sigma$ range about the mean in the size distribution. Optical microscope scan measurements (at the University of Kent) and SEM images (Natural History Museum, London) of all the bead samples sizes were taken to test their size distribution, for example figure 5. The histograms and statistical analyses of the projectile samples (Figure 6, with sample

sizes given in Table 1) show that most have a tight clustering of size around a single size mode within 1σ of the mean value as supplied by Whitehouse Scientific, but in some cases the distributions had greater dispersion than specified. For example, the smallest sphere sample employed (Figure 5) had a much broader range of projectile dimensions, with many of sizes down to 50% of the mode dimension. In the larger bead samples, some small grain protrusions were evident (c. 10% of beads) and 5% of beads were smaller than expected. There were very few broken beads, although the crater size distribution does suggest that some projectiles did fragment during the violent acceleration to impact velocity. Nevertheless, the measured glass projectiles yielded an easily determined size calibration, with average diameters and standard deviations given in table 1, and used in the following analysis.

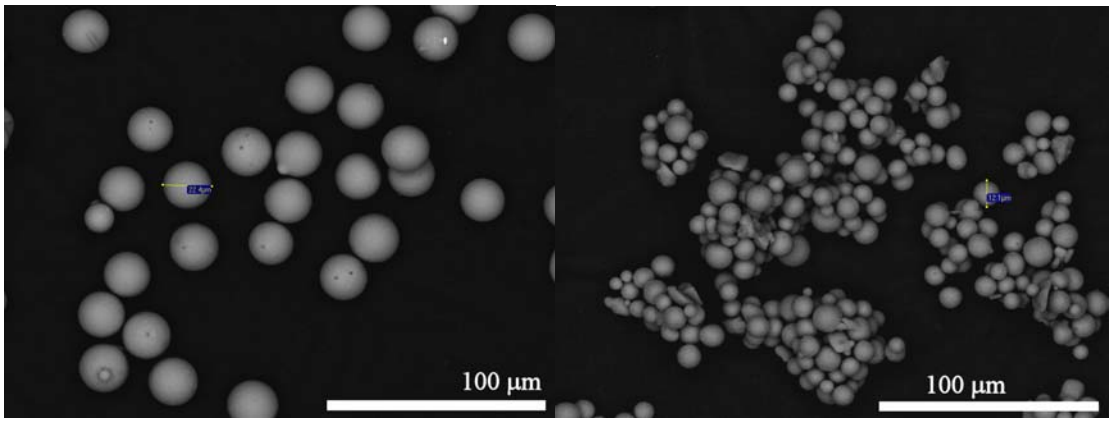

Figure 5. Backscattered electron images of soda lime glass bead projectiles, showing uniform size in the nominal 22.8 micron sample (left), but broader distribution in the nominal 11.58 micron sample (right). Note digital measurement calipers on images.

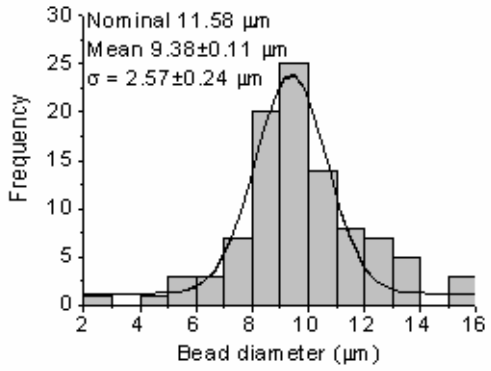
Nominal 11.58 µm
Mean 9.38±0.11 µm
σ = 2.57±0.24 µm
Frequency
Bead diameter (µm)

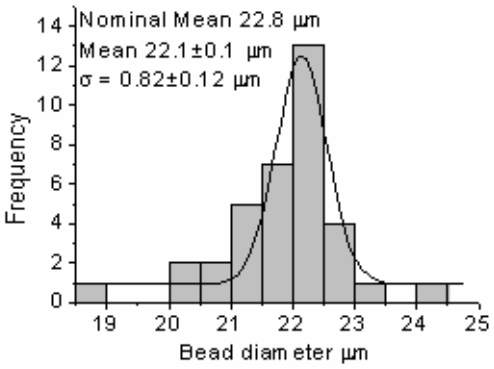
Nominal Mean 22.8 µm
Mean 22.1±0.1 µm
σ = 0.82±0.12 µm
Frequency
Bead diameter µm

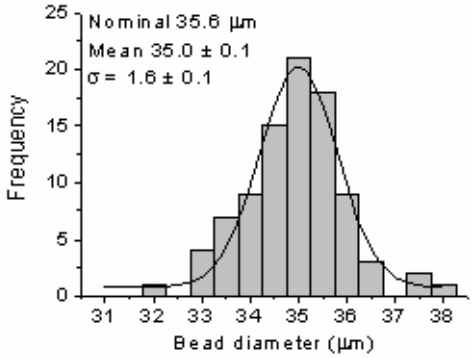
Nominal 35.6 µm
Mean 35.0 ± 0.1
σ = 1.6 ± 0.1
Frequency
Bead diameter (µm)

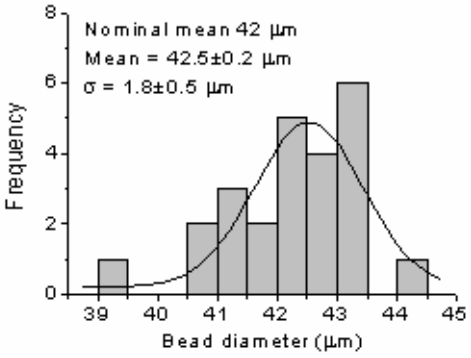
Nominal mean 42 µm
Mean = 42.5±0.2 µm
σ = 1.8±0.5 µm
Frequency
Bead diameter (µm)

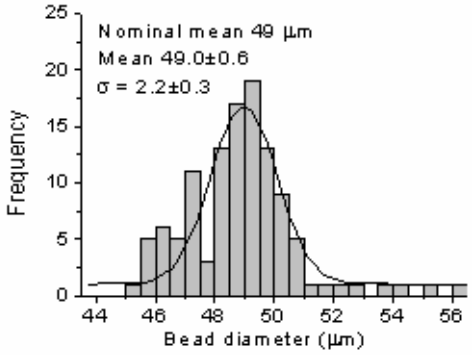
Nominal mean 49 µm
Mean 49.0±0.6
σ = 2.2±0.3
Frequency
Bead diameter (µm)

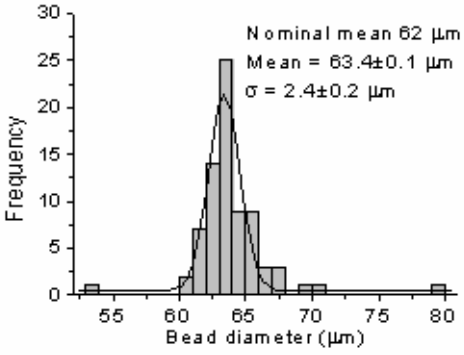
Nominal mean 62 µm
Mean = 63.4±0.1 µm
σ = 2.4±0.2 µm
Frequency
Bead diameter (µm)

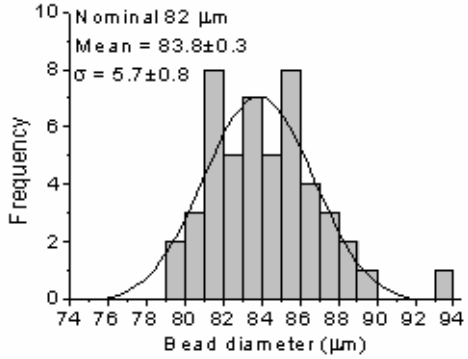
Nominal 82 µm
Mean = 83.8±0.3
σ = 5.7±0.8
Frequency
Bead diameter (µm)

Figure 6. Particle diameter histograms for the soda lime glass bead projectiles used for light gas gun shots at NASA and Kent. Absolute numbers of projectiles are plotted, with sample sizes given in Table 1.

Experimental shot programme

Light gas gun shots were performed in two separate facilities: at the University of Kent in Canterbury, England (Burchell *et al*., 1999), and at the Johnson Space Centre of the National Aeronautics and Space Administration (NASA) in Houston, Texas, USA. Both laboratories used similar small calibre two stage light gas guns with many common features. The gun barrel bore was 5mm (NASA) and 4.3 mm (Kent). The guns employed a variety of mechanical apertures, a sabot catcher system and (NASA gun only) flapper valves that minimized the contamination on the target site by fine grained debris from a variety of sources (high pressure piston, stainless steel burst diaphragm, gun barrel, and sabot catcher). On each gun, independent velocity measurement stations, using combinations of laser occultation methods, IR photo diodes and impact momentum sensors, determined the velocity of the sabot pieces; additionally, in the NASA gun, the actual projectile arrival at the target site was monitored by an impact flash detector, i.e. another photo diode. Typically, sabot velocity and projectile velocity agreed to better than 1% (NASA) and 2% (Kent). The intended speed in each shot was 6.1 km s^{-1}, the nominal Stardust encounter speed at comet P/Wild2. There were slight variations from shot to shot, and the measured speed for each is given in table 1.

It is not practical with light gas guns to launch individual particles < 250 um, this is the reason why all projectiles employed in this paper were “shot gunned” or “buckshot”, i.e. launched as an ensemble of projectiles. Depending on projectile size, some tens to hundreds of individual particles were loaded into a small, central cavity of a 4-piece, serrated sabot (both guns used similar sabots). By design, the 4 sabot quadrants separated radially during free flight, yet allowed a substantial fraction of the projectile ensemble to remain on straight trajectories and to ultimately reach the target site. A number of mechanical apertures assured that only those particles that resided within < 1 degree of the gun axis reached the target; all others were terminated by mechanical apertures, including the sabot pieces. During each shot the target chamber was evacuated to typically a few 10^{-1} mbars or better.

The foil target was held upon a massive aluminium plate. At NASA, Al 6061-T6 was used (the same grade as the Stardust frame on which the foils are mounted in space), some 2.47 cm (1”) on the side and 0.62 cm (1/4”) thick. At Kent Al 6068 was used (Al 6068 is an alloy with similar physical properties to Al 6061) some 1.5 x 1.5 cm across and 0.2 cm thick. These plates were wrapped as tightly as possible, using pliers, with the thin aluminium foil. The foil was 100 μm thick (4/1000” nominal), made of aluminium 1100, but of unknown temper grade and annealing history; however, the foil used and kindly supplied by P. Tsou, JPL, was from exactly the same batch that was also used on the Stardust mission. This target arrangement resembled the basic Stardust instrument configuration and materials to permit high fidelity comparative experiments. Once wrapped, targets were placed in the gun. For example, at Kent they were secured to a larger aluminium (HE30) plate (10 x 10 cm) for mounting in the gun, as shown in Figure 7. Two shots were also performed at Kent on the Al 1100 foil suspended with a free rear surface, to test the influence of the mounting on crater size and foil penetration. In addition, an extra control shot was done (at Kent), which used the same target as normal, but no projectiles were loaded

in the sabot. This provided a target surface which had been exposed to the gun environment during a shot and which could be used as a baseline reference for determination of gun artifacts.

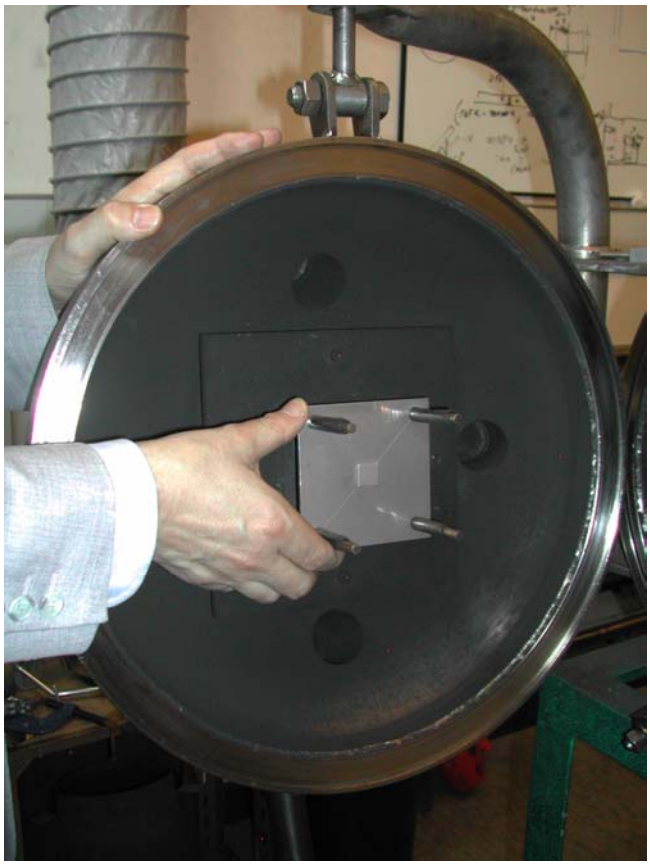

Figure 7. A foil-wrapped 15mm plate, mounted upon an aluminium base-plate (drilled with four locating holes for support), is placed on the target holder in the light gas gun chamber at Kent.

IMPACT FEATURES AND THEIR MEASUREMENT

To ensure comparability of datasets between laboratories that will participate in the Stardust foils analysis, and by common agreement among those that constitute the Stardust Preliminary Investigation Team, it was decided that impact feature measurements should be based on the crater diameter as defined by intersection with a projected horizontal surface laid upon the raised crater lip (figure 8). This measured dimension is equivalent to the crater diameter (D) as employed in studies of impacts on the Long Duration Exposure Facility by e.g. See et al. (1994). High precision measurements of the crater inner diameter and the crater depth relative to the level of the ambient metal surface can be performed by stereometry of multiple SEM images with known angular separation, although the process is very laborious for a large number of craters on an extensive flat surface, even with modern processing routines. Similarly, the shallow depth of focus of most optical microscopes allows relatively easy measurement of the crater internal diameter at the ambient plane, but has a lower spatial resolution than SEM techniques. However, the narrow dispersion of crater diameter to depth ratios seen in micrometeoroid impact craters on LDEF (Love et al.,

1995) and the relatively modest control of crater morphology by projectile density at >6 kms^{-1} (Humes, 1991), suggests that the size of a single crater feature such as D may suffice for determination of particle size, especially if there is a narrow range of impact velocities, as in the case of the Stardust encounter. Nevertheless, there is evidence that different particle compositions may yield different impact penetration depths (Wallis et al., 2002), and as part of our continuing research we are investigating the role of specific particle characteristics in controlling crater morphology.

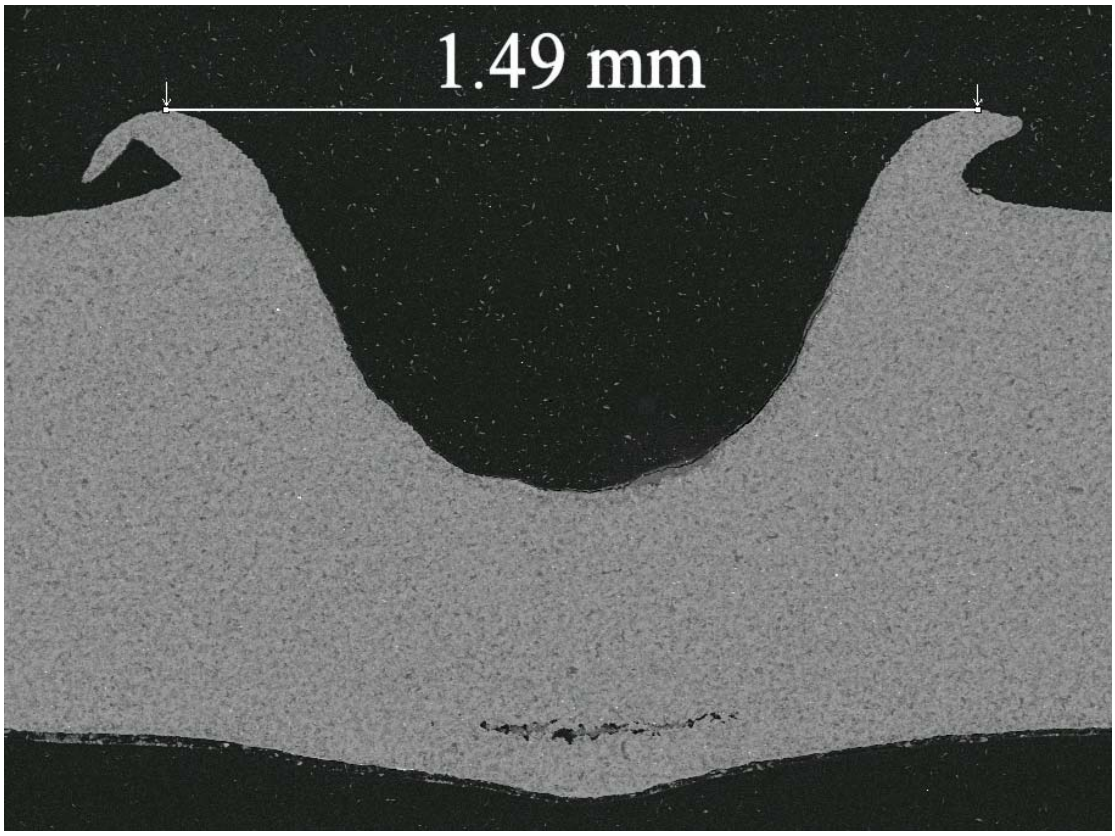

Figure 8. Backscattered electron image of a vertical section through an impact crater on aluminium. Crater diameter is defined as length of the horizontal line indicated.

Secondary electron images (SEI) taken perpendicular to the foil surface show complex textures on the crater lip, and it can be difficult to recognise the proper point at which to draw the end of the measurement callipers. On some craters, it may be easier to locate appropriate points for measurement by use of backscattered electron imagery (BEI). The geometric position of the solid-state BE detector in the JEOL 5900 sample chamber (an annular ring around the lower aperture of the objective lens) results in a maximum signal level from surfaces that are perpendicular to the electron beam incidence. This detector location intersects the path of numerous, high energy electrons that have undergone high angle scattering from the dense metal. Surfaces that are inclined to the electron beam (such as the crater interior wall and the inclined margins of the crater lip) will appear darker in BEI due a greater proportion of the energetic beam electrons being scattered at an angle away from the small, localised detector (figure 9). It is therefore relatively easy to locate the mid point between the outer lip slope and the crater pit wall in BEI, and to utilise this location as the standard measurement point.

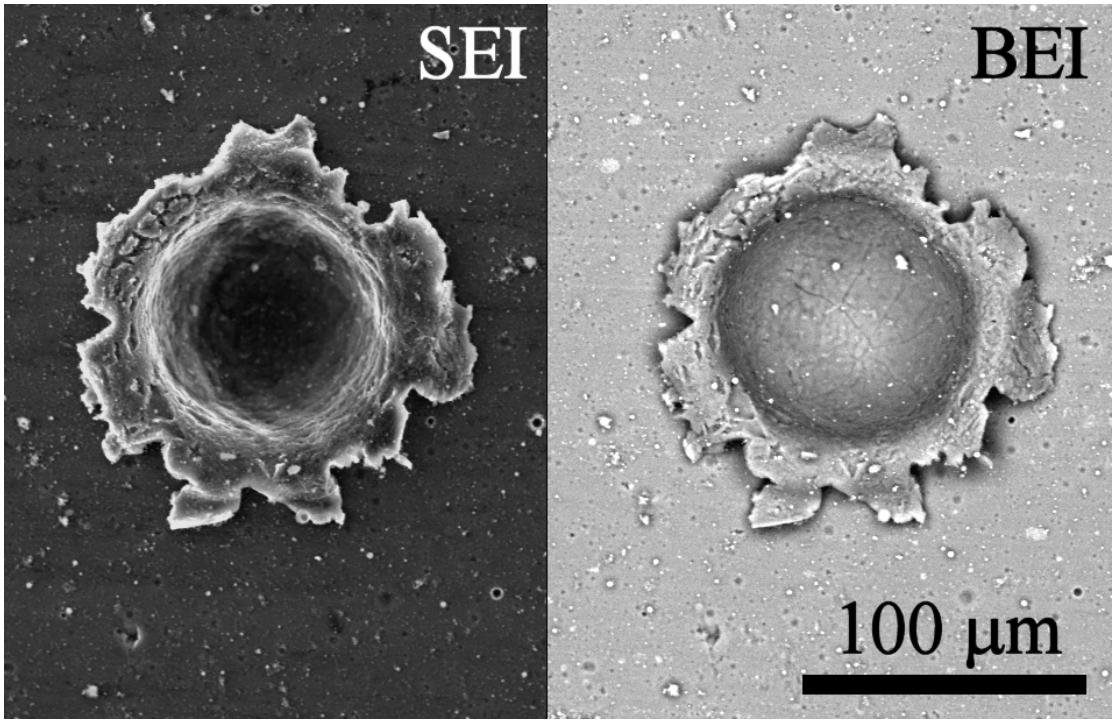

Figure 9. Comparison of secondary electron (left) and backscattered electron images (right) showing topographic contrast used to define horizontal surface of crater lip.

For this calibration study, three measurements were taken from each crater that possessed an intact, continuous uplifted oval to circular rim, with an angular spacing of approximately 60 degrees (figure 10). Overlapped impact features (uncommon on most targets) were not included in the dataset as their dimensions may reflect interference between crater-forming events on a damaged substrate. On features with incomplete rims, two or occasionally only one measurement could be taken. The average diameter value for each crater was tabulated and is plotted in the bins shown on the histograms of figures 11 and 12.

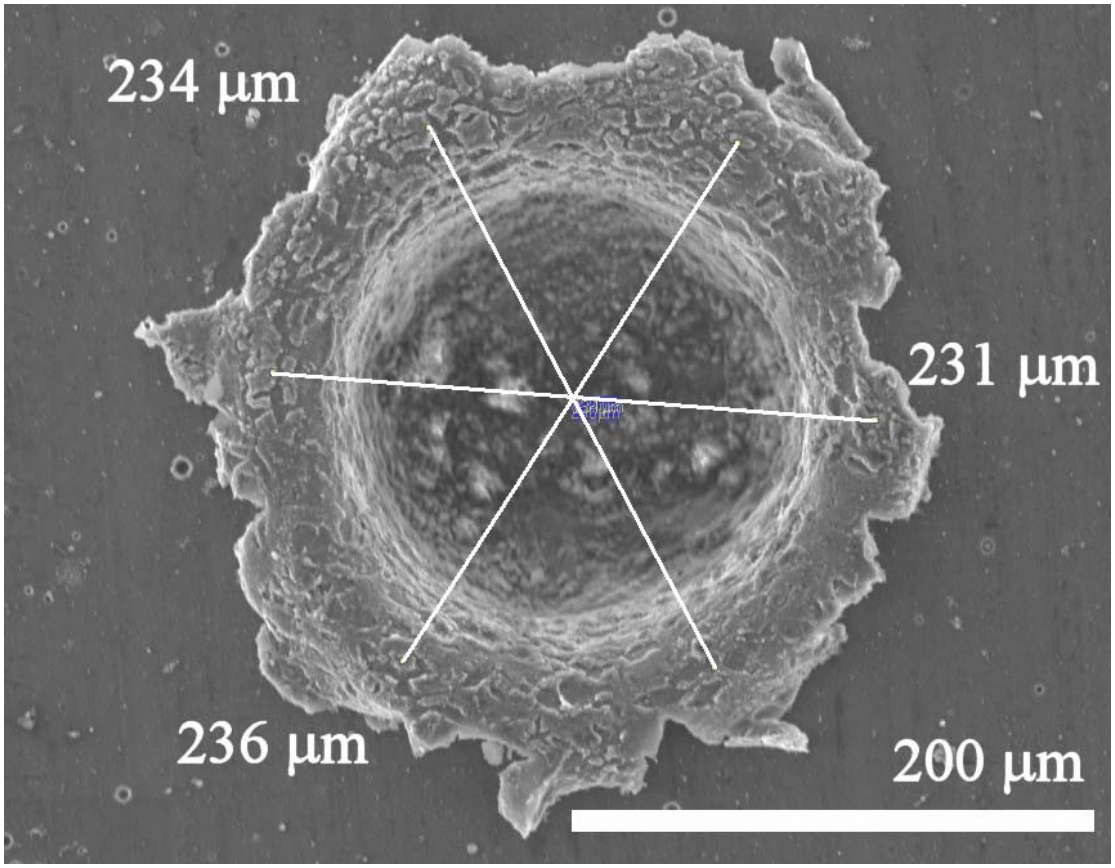

Figure 10. Secondary electron image of a crater produced by impact of a grain of the pyroxene enstatite on Stardust foil. The lines of three diameter measurements by digital callipers are shown.

Results from projectile and impact feature size measurement

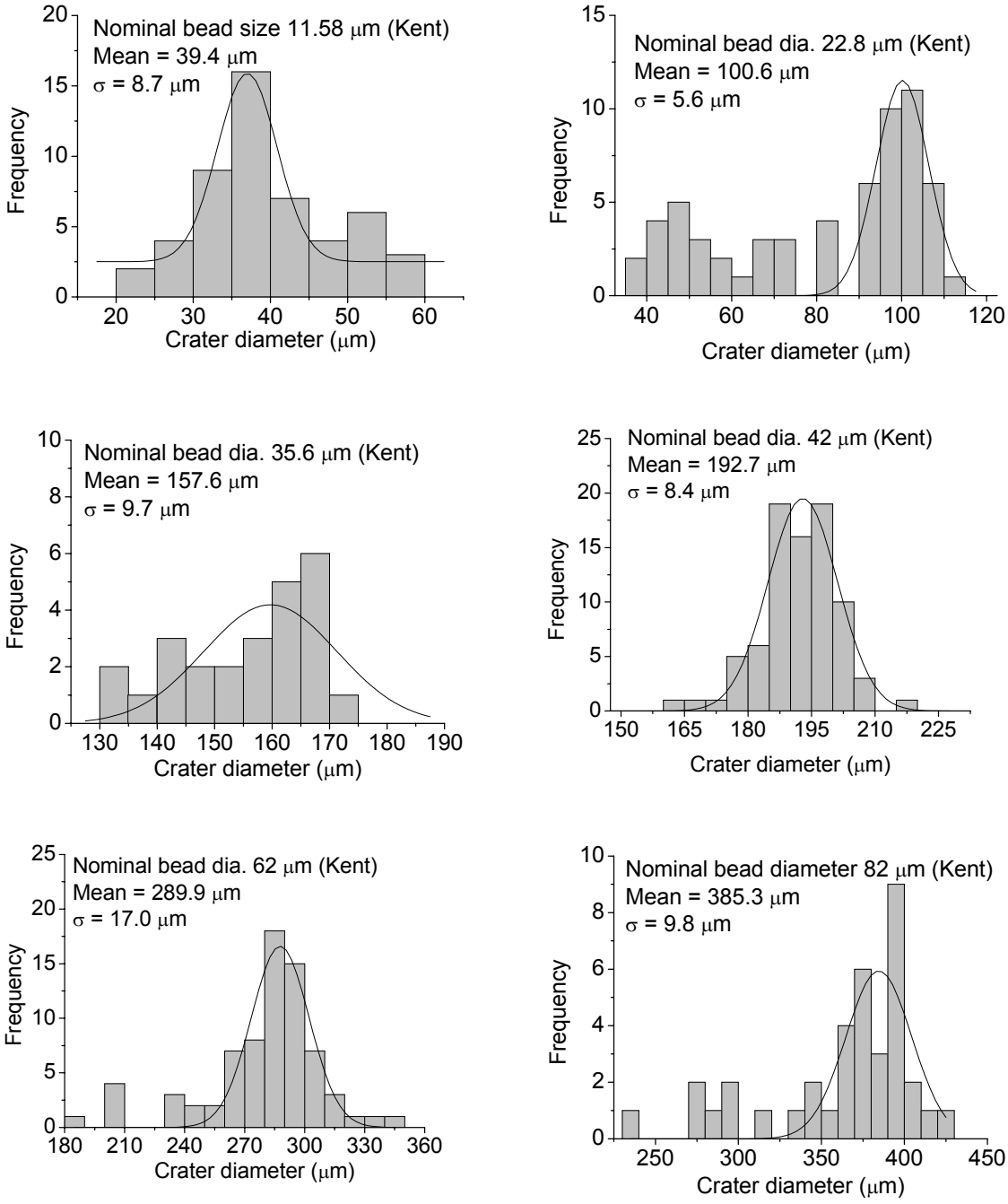

Figure 11. Impact crater diameters (Kent), showing full raw size distribution and population above 4 times projectile diameter, selected for calibration plot in figure 13.

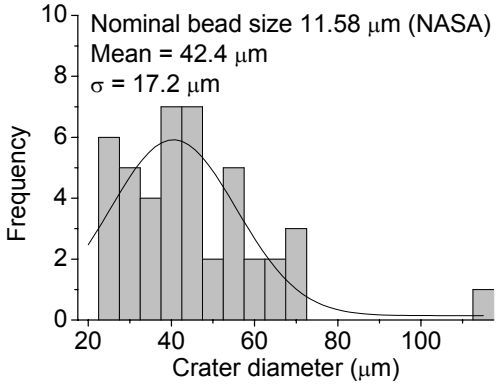
Nominal bead size 11.58 μm (NASA)
Mean = 42.4 μm
σ = 17.2 μm
Frequency
Crater diameter (μm)

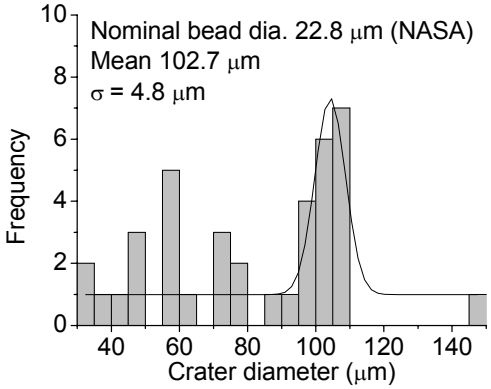
Nominal bead dia. 22.8 μm (NASA)
Mean 102.7 μm
σ = 4.8 μm
Frequency
Crater diameter (μm)

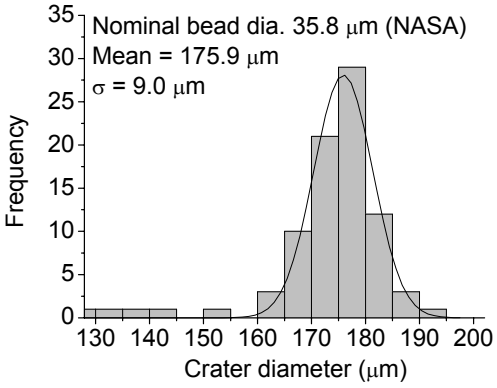
Nominal bead dia. 35.8 μm (NASA)
Mean = 175.9 μm
σ = 9.0 μm
Frequency
Crater diameter (μm)

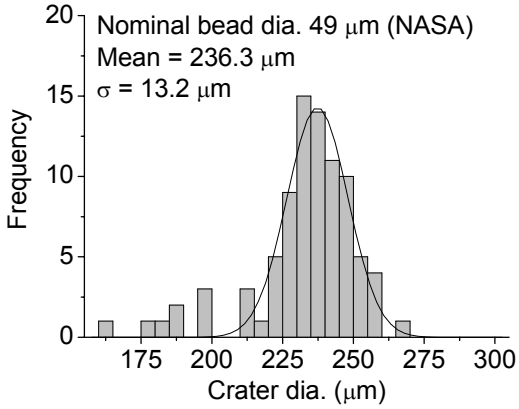
Nominal bead dia. 49 μm (NASA)
Mean = 236.3 μm
σ = 13.2 μm
Frequency
Crater dia. (μm)

Figure 12. Impact crater diameters (NASA), showing full raw size distribution and population above 4 times projectile diameter, selected for calibration plot in figure 13.

We have omitted the very smallest craters (of less than 15 microns, and therefore less than twice the peak minimum glass bead diameter) from the statistics as they appear on target foils throughout the shots, including the blank sabot shot, and we believe them to represent fine gun debris and fragmented projectiles.

Two notable features stand out in each of the histograms in figure 11: concentration of crater dimensions into a peak between four and five times the projectile diameter; and a substantial 'tail' of smaller craters. The projectile size range determined by calibrated SEM imagery of each glass sphere sample does show some dispersion around the nominal size peak (figure 6), especially in the smallest particles, but insufficient to account for the 'tail' on the lower size shoulder of the crater size mode. Our in-situ measurements of projectile velocity show little dispersion (± 2%) within a shot and, we therefore attribute these smaller craters to impacts by fragmented projectiles. On the Stardust foils, of substantially greater thickness than the diameter of our projectiles, there seems to be relatively little influence of subtle differences in particle shape on crater circularity. There is no correlation between abundance of smaller craters and irregular shape, hence the small variation in crater maximum/minimum diameters, shown in the final column of table 1. Our preliminary results from a survey of impacts by markedly inequant pyroxene grains with a high shape factor (i.e. a rod or plate morphology) onto Stardust foils does not show a greater range of crater outline shape than seen in the glass bead shots, and we therefore regard crater shape on such foils as relatively insensitive to projectile form. However, impacts onto much thinner foils may preserve a closer proxy to the projectile size and shape as the particles pass through the full foil thickness, and we intend to perform this experiment to verify projectile fragmentation. Shots of the same projectiles into aerogel targets do show evidence of some particle fragmentation but whether during acceleration and flight to the target or on impact is unknown. In conclusion, although the impact craters may reflect the particle size distribution encountering the target, they probably do not give a perfect representation of the particle size distribution in the sabot before firing.

This artefact of the extremely high acceleration in light gas gun shots will not be a factor in the creation of cometary particle impacts on the Stardust spacecraft, where dimensions are expected to be a simpler reflection of the impacting particle size distribution. However, for a suite of calibration experiments it is necessary to exclude data from projectile fragments of unknown size. We present the raw size data in Table 1, and statistics for crater diameters above a minimum threshold value of 4 times the projectile modal diameter (superimposed graphs and data in figures 11 and 12) as the lower limit for inclusion within the sample plotted on the calibration graph for the metal-wrapped foil shots (figure 13). Filtering of the data set by this threshold leads not only to an inevitable reduction in standard deviation, but also a marked improvement in the quality of linear regression fit to a straight line. For almost all the crater size distributions, the exclusion of data from less than 4 times the projectile size does not impinge upon the mode seen in the histograms, except for the smallest projectile sample where this cut-off point is within the substantial small-size shoulder of the mode, reflecting the wide range of sizes in this projectile sample. In the analysis we therefore do not apply this cut on the data for the impact craters from the smallest projectile sample. However, it is notable that following imposition of the 4 times diameter filter, all of the point plots from twelve shots, including shots from

both NASA and Kent laboratories, fall within one standard deviation of the linear fit. There is thus demonstrable linear proportionality between projectile diameter and resulting crater diameter. As particle mass should be proportional to the cube of the projectile radius, this gives a mass dependent exponent of 0.333, close to the 0.352 determined experimentally by Humes (1991). Variation in impact velocity between shots (from 5.85 kms^{-1} to 6.22 kms^{-1}, see table 1) appears to have had little systematic effect upon crater dimensions, again in accordance with the empirical equations of Humes (1991), with the velocity dependent exponent likely to give crater size dispersion of less than 3% relative.

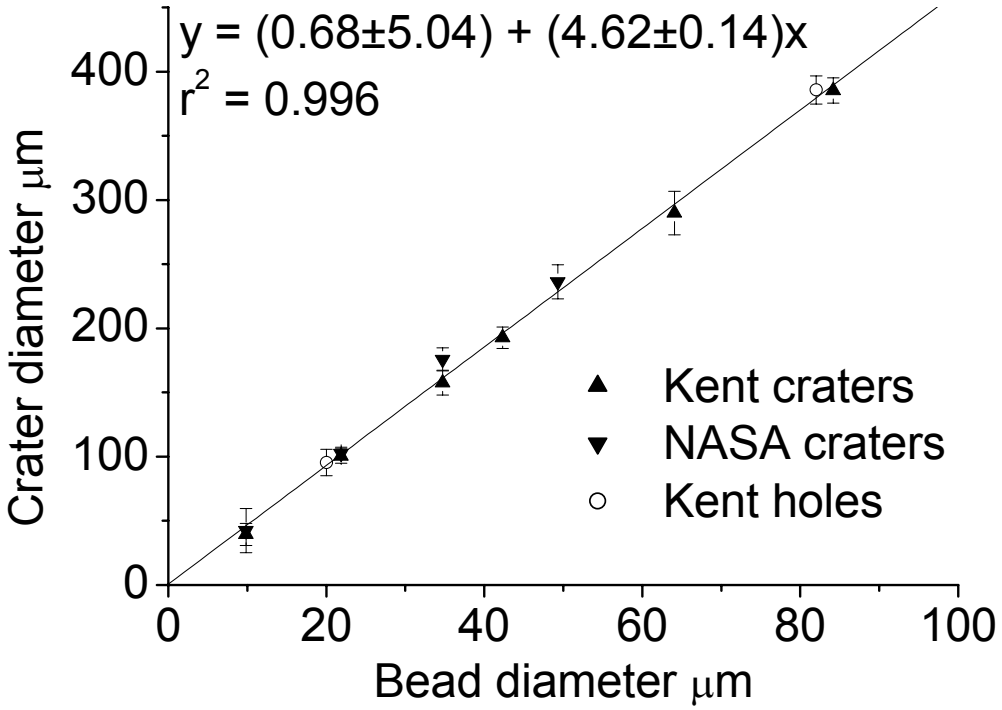

Figure 13. Crater diameter vs. bead diameter. The fit shown is to the combined Kent and NASA crater data sets. Also shown are crater lip to lip diameters of the holes in the un-supported foils impacted at Kent, offset slightly to the left of their true plot position on the bead projectile axis, as otherwise they overlap the other data and would be indistinguishable.

We therefore consider that the most appropriate calibration equation for craters created by impacts onto 100 micron Al1100 foil at around 6.1 kms^{-1} by particles between 10 microns and 80 microns in diameter and with the density of glass, is the best fit of figure 13:

Impacting particle diameter = Impact crater diameter / 4.62 eqn (1)

DISCUSSION AND FUTURE WORK

There are a number of potential sources of error in this calibration study which require discussion.

The complexity of image tone distribution is not suited to automated image processing and appropriate placement of calipers on stored digital images has to be performed manually. In the reported study, all of the imagery and measurement was performed by one person (ATK) and hence perception of the correct features may be considered consistent throughout. Images with a relatively low number of pixels spanning the feature of interest (e.g. small craters or spheres) inevitably compromise measurement precision, although repeated measurements from the same crater do yield reproducible location of points, and the range of individual measurements for the three diameters is small, typically less than 5% dispersion between the crater maximum and minimum diameter average (see final column of table 1).

Incomplete edge 'turn-over' and detachment of extensive segments of the rim was observed in some craters, limiting the number of diameter measurements that could be made reliably. However, careful handling of the foils ensured that no surface flattening occurred, as this might depress the curved portion of the crater lip and thereby change the apparent crater diameter measurement. The handling of impacted soft aluminium foils during sample extraction from the Stardust aerogel collector may also generate a suite of crater dimension modifications, due to localised shortening during bending to produce an approximately planar sheet, and craters in these regions of the foil should be examined with care. Although the majority of crater rims approximated a circular plan outline in backscattered electron images with beam normal incidence, secondary electron imagery did sometimes reveal more complex subsurface morphology. A few craters (31/433 craters with three diameters measured) display oval rim outlines, defined herein as maximum/minimum diameter exceeding 1.10, but none exceeded 1.19. Deviations from perfect circularity may have complex sources that are difficult to track down, but may include non-spherical impactors, spheres with protuberances and spheres containing bubbles (all observed in the optical microscope), as well as variation in the size and orientation of target crystals and impact proximity to associated grain boundaries.

The 'blank' shot at Kent, using an empty sabot, demonstrated that the light gas gun itself yields only a very small number of impacts from mobilised gun components (such as the burst disk, high pressure piston or sabot) generating craters of a size comparable to the smallest glass bead projectiles. Although there are numerous craters of less than 20 microns in diameter, we suggest that there is no significant contribution from mobilised parts of the apparatus to the numbers of craters in our calibration plot.

Comparison of craters from tightly-wrapped foil to those on foils with a rear free surface shows that variation in the proximity of the foil to the underlying frame will have a minor effect. Two shots, with 21.87 and 84.14 micron determined particle diameters, were taken with free rear surface targets. In both cases there is a small increase in the crater diameter over shots with tightly wrapped foil, but with the standard deviation still overlapping the linear fit to the entire dataset. As these were 'worst-case' situations, with no physical coupling to the underlying aluminium frame, we consider that variation in the tightness of foil wrapping will not seriously compromise application of our calibration data to the Stardust spacecraft. Interestingly, we note that in both cases, the spread on the observed crater size was significantly reduced compared to the shots where the targets were mounted flush with a supporting substrate.

Comparability of projectiles to micrometeoroid materials.

In this paper we have shown that there is a simple relationship between impacting particle diameter and the width of the crater produced on Stardust foils (impacting particle diameter = impact crater diameter / 4.62). What factors might cause cometary particle impacts to deviate from this simple scale relationship?

Experimental measurements of aluminium target crater formation under closely controlled conditions, reported in previous studies (e.g. Cour-Palais, 1987) have shown that crater dimensions such as depth are dependent upon particle mass, density, velocity and impact incidence angle (but see below). For instance, Humes (1991):

Crater depth below ambient surface = 0.42*(particle mass$^{0.352}$)*(particle density$^{0.166}$)*(particle velocity$^{0.666}$)*(cosine of incidence angle$^{0.666}$). eqn (2)

Our experiments used spherical glass projectiles of 2.4 gcm^{-3}density, similar but somewhat greater than that determined for cometary dust particles (c. 2.0 gcm^{-3}, Love et al., 1994; 1.6 to 2.4 gcm$^{-3,}$ McDonnell and Gardner, 1999), but less than that determined by Burchell et al., 1998 for particles impacting spacecraft in LEO (3.4 gcm^{-3}). However, the small value of the density exponent in the equation above suggests that crater diameter should be relatively insensitive to density differences between glass and silicate micrometeoroid particles. Although the mineral composition and fine structure is as yet unknown from pristine samples collected in space, there is extensive literature on both remote sensing of cometary dust by infrared spectrophotometry (e.g. Wooden et al., 1999) and the composition and structure of delicate interplanetary dust particles captured in the stratosphere (see review by Rietmeijer, 1998). Both suggest that many dust particles will contain porous aggregates of small grains of silicates including the pyroxene enstatite (σ = 3.2 gcm^{-3}) and forsterite olivine (σ = 3.2 gcm^{-3}) as well as iron sulfides (σ = 3.2 gcm^{-3}), amorphous silicates and organic matter of density around 1 gcm^{-3}. Although it is important to utilise projectiles that will produce similar impact effects to those expected to be generated by cometary particles, it is not possible to simulate these fragile aggregates, and we await examination of the returned foils to determine whether shallow, broad and irregular impact features may indicate very low density and complex grain impacts. Nevertheless, we have performed impact experiments with enstatite and olivine, among other minerals, and have begun initial analysis of the role of inequant particle shape on crater dimensions.

Love et al. (1995) demonstrated that there is relatively little variation in the ratio of crater depth to diameter in micrometeoroid impact craters of a wide range of sizes upon LDEF space-facing substrates. It is therefore reasonable to assume that for silicate-dominated particles there is a similar crater diameter relationship to impacting particle parameters. However, Wallis et al. (2002) demonstrated that for impacts onto aluminium, by mineral grains at a speed of 5.3 kms^{-1}, there may be substantial variation in the shape of impact features as a function of particle characteristics, especially density and hardness, and that depth may no longer be at a constant ratio to crater diameter. Hörz et al., 1993 have shown that laboratory impact experiments can yield important projectile size calibration data for aluminium foils, but to date, no extensive calibration of crater shape dependence upon particle physical properties has

been published for impacts onto substrates akin to the Stardust foils by particles analogous to cometary minerals.

To address this issue, five other foil shots were also performed at Kent, using projectiles of: (1) crushed Orgueil C1 carbonaceous chondrite meteorite; (2) a mixture of olivine (38 – 53 microns by sieving) and Al_2O_3 grains (typically 3 microns); (3) pyroxene (enstatite) less than 38 microns (sieved); (4) crushed basalt glass from an analytical test sample from the United States Geological Survey and (5) a mixture of enstatite, olivine, diopside, anorthite, pyrrhotite, magnetite, calcite, Orgeuil fragments, and 22 micron soda-lime glass spheres. These provided analogue samples for compositional analysis of impact residues under a range of original projectile size, shape, chemical composition, density, hardness etc., and will be described in a further publication. Accurate 3 dimensional crater-shape determination is a difficult and time-consuming process, although modern stereometry routines such as MEX, marketed by Alicona, may allow precise feature measurement (e.g. figure 14), including determination of crater profile, depth and width at the plane of the ambient foil surface.

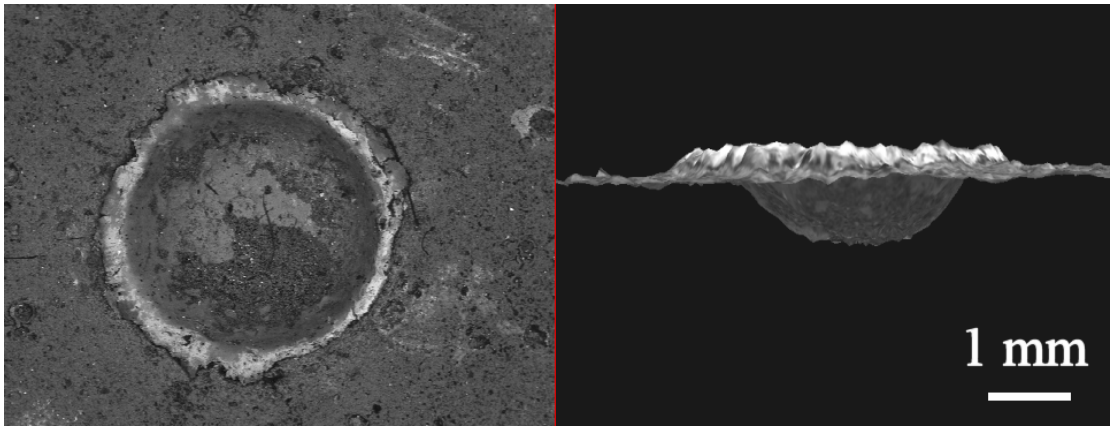

Figure 14. Backscattered electron image of an impact crater on titanium metal (left), and projection of a three dimensional digital model derived from tilted inclination images of the same crater (right). It is possible to measure both crater depth below, and crater inner diameter at the ambient target surface. Reconstruction using MEX software, courtesy of Alicona Imaging GmbH.

Conclusion

A robust calibration for impactor size vs. impact crater size has been obtained for the aerogel mounting foils carried by the Stardust return capsule. This covers a wide size range of interest (impactor sizes c. 10 to 85 microns). Extrapolation of the size calibration presented in this paper to a projectile diameter of 1 micron is probably acceptable, but for smaller sizes it may be necessary to use other types of accelerators and projectiles (e.g. Goldsworthy, 2002) and simulations of impact for nanometre-scale particles (e.g. using numerical molecular dynamics such as the SPaSM code of Beasley and Lomdahl, 1994). For particles larger than 100 microns diameter, it is important to note the potential role of the discontinuity at the rear of the foil, and possible poor mechanical coupling with the underlying Al 6061 frame. Should craters of greater than 400 microns diameter be observed on Stardust foils, it may be helpful to perform more shots, with larger projectiles than were used in this study. In

conclusion, a reasonably reliable and independent estimate of the impactor size flux can be obtained from the observed crater size distribution on the Stardust foils.

Acknowledgements – We thank The Natural History Museum London for access to electron microscope facilities; Nick Foster (Univ. of Kent) for information on glass sphere projectile fragmentation from impacts onto silica aerogel. The JSC experiments were supported by Stardust Project funds.

REFERENCES

Beasley D. M and Lomdhal P. S. (1994) Message-passing multi-cell molecular dynamics on the Connection Machine 5. *Parallel Computing* **20**, 173-195.

Bernhard R. P. and Hörz F. (1995) Craters in aluminium 1100 by soda-lime glass spheres at 1 to 7 km/s. *International Journal of Impact Engineering* **17**, 69–80.

Bernhard R. P., Durin C. and Zolensky M. E. (1994a) Scanning Electron Microscope/ Energy Dispersive X-ray analysis of impact residues in LDEF tray clamps. In: *LDEF- 69 months in space, NASA Conference publication 3194. Part 2* (ed. A. S. Levine), pp. 541-549. National Aeronautics and Space Administration, Washington, D.C., USA.

Bernhard R.P, See T.H. and Hörz, F. (1994b) Projectile compositions and modal frequencies on the "Chemistry of Micrometeoroids" LDEF experiment. In: *LDEF- 69 months in space, NASA Conference publication 3194. Part 2* (ed. A. S. Levine), pp. 551-573. National Aeronautics and Space Administration, Washington, D.C., USA.

Brownlee D. E., Joswiak D., Bradley J.P. and Hörz, F. (1994) Interplanetary meteoroid debris in LDEF metal craters. In: *LDEF- 69 months in space, NASA Conference publication 3194. Part 2* (ed. A. S. Levine), pp. 577-584. National Aeronautics and Space Administration, Washington, D.C., USA.

Brownlee D. E., Tsou P., Anderson J.D., Hanner M.S., Newburn R.L., Sekanina Z., Clark B.C., Hörz F., Zolensky M.E., Kissel J., McDonnell J.A.M., Sandford S.A., and Tuzzolino A.J. (2003) Stardust: Comet and interstellar dust sample return mission. *Journal of Geophysical Research (Planets)* **108(E10),** 8111, 10.1029/2003JE002087.

Burchell M.J. and Mackay N. (1998) Crater Ellipticity in Hypervelocity Impact On Metals. *Journal of Geophysical Research* **103 E**, 22761-22774.

Burchell M.J., Cole M.J., McDonnell J.A.M., Zarnecki J.C. (1999) Hypervelocity Impact Studies Using the 2 MV Van de Graaff Dust Accelerator and Two Stage Light Gas Gun of the University of Kent at Canterbury. *Measurement Science and Technology* **10**, 41-50.

Christiansen E., Cykowski E. and Ortega J. (1993) Highly oblique impacts into thick and thin targets. *International Journal of Impact Engineering,* **14,** 157-168.

Cour-Palais B. G. (1987) Hypervelocity impacts in metals, glass and composites. *International Journal of Impact Engineering* **5**, 681-692.

Davis J. R. (ed.) (1998) *Metals Handbook. Desk Edition (Second Edition*). ASM International, Materials Park, Ohio, USA.

Dunn B. D. (1997) *Metallurgical assessment of spacecraft parts, materials and processes, 2nd Edition*. John Wiley and Sons, Chichester, West Sussex, UK.

Goldsworthy B. J., Burchell M. J., Cole M. J., Green S. F., Leese M. R., McBride N., McDonnell J. A. M., Müller M., Grün E., Srama R., Armes S. P. and Khan M. A. (2002) Laboratory calibration of the Cassini cosmic dust analyzer (CDA) using new, low density projectiles. *Advances in Space Research* **29**, 1139-1144.

Graham G. A., Kearsley A. T., Wright I. P., Grady M. M., Drolshagen G., McBride N. M., Green S. F., Burchell M. J., Yano H. and Elliott R. (2001) Analysis of impact residues on spacecraft surfaces: possibilities and problems. In *Proceedings of the 3rd European Conference on Space Debris: ESA Special Publication **473*** (ed. H. Sawaya-Lacoste), pp.197-203. ESA Publications Division, ESTEC, Noordwijk, The Netherlands.

Graham G. A., Kearsley A. T., Drolshagen G., McDonnell J. A. M., Wright I. P. and Grady M. M. **(**2004) Mineralogy and microanalysis in the determination of cause of impact damage to spacecraft *surfaces. In Forensic Geoscience: Principles, Techniques and Application*: *Special Publication 232.* (eds. K. Pye and D. J. Croft), pp. 137-146. The Geological Society of London, London, UK.

Graham G.A., Sheffield-Parker J., Bradley J.P., Kearsley A.T., Dai Z.R., Mayo S.C., Teslic, N., Snead C., Westphal A.J., Grant P.A. and Ishii H.A. (2005) Electron beam analysis of micrometeoroids captured in aerogel as stardust analogues (abstract). *Lunar and Planetary Science Conference* **XXXVIth,** #2078.

Grün E., Fechtig H., Giese R. H., Kissel J., Lindblad B.-A., Linkert D., Maas D., McDonnell J. A. M, Morfill G. E., Schwehm G. and Zook H. A. (1992) The Ulysses dust experiment. *Astronomy and Astrophysics Supplement Series* **92.2**, 411-423.

Grün E., Baguhl M., Divine N., Fechtig H., Hamilton D.P., Hanner M.S., Kissel J., Lindblad B.-A., Linkert D., Linkert G., Mann I., McDonnell J.A.M., Morfill G.E., Polansky C., Riemann R., Schwehm G., Siddique N., Staubach P. and Zook H.A. 1995 Three years of Galileo dust data. *Planetary and Space Science Review* **43**, 953-969.

Hörz F., Cintala M., Bernhard R. P. and See T. H. (1993) Dimensionally scaled penetration experiments to extract projectile sizes from space exposed surfaces. *International Journal of Impact Engineering* **14**, 347-358.

Hörz F., Zolensky M. E., Bernhard R. P., See T. H. and Warren J. L. (2000) Impact Features and Projectile Residues in Aerogel Exposed on Mir, *Icarus* **147**, 559 – 579.

Humes D. H. (1991) Large craters on the meteoroid and space debris impact experiment. In: *LDEF- 69 months in space, NASA Conference publication 3134. Part 1* (ed. A. S. Levine), pp. 399-418. National Aeronautics and Space Administration, Washington, D.C., USA.

Kearsley A. T., Drolshagen G., McDonnell J. A. M., Mandeville J.-C. and Moussi A. (2005) Impacts on Hubble Space Telescope solar arrays: discrimination between natural and man-made particles. *Advances in Space Research* **35**, 1254-1262.

Kissel J., Glasmachers A., Grün E., Henkel H., Höfner H., Haerendel G., von Hoerner H., Jessberger E. K., Krueger F. R., Möhlmann D., Greenberg J. M., Langevin Y., Silén J., Brownlee D., Clark B. C., Hanner M. S., Hörz F., Sandford S., Sekanina Z., Tsou P. Utterback N. G., Zolensky M. E. and Heiss C. 2003. Cometary and Interstellar Dust Analyzer for comet Wild 2, *Journal of Geophysical Research* **108(E10),** 8114, 10.1029/2003JE002091.

Love S. G., Brownlee D. E., King N. L. and Hörz F. (1995) Morphology of meteoroid and debris impact craters formed in soft metal targets on the LDEF satellite. *International Journal of Impact Engineering* **16,** 405–18.

Love S.G., Joswiak D.J. and Brownlee, D.E. 1994 Densities of stratospheric micrometeorites. *Icarus* **111**, 227-236.

McDonnell J. A. M. and Gardner D. J. (1998) Meteoroid morphology and densities: decoding satellite impact data. *Icarus* **133**, 25-35.

Moussi A., Drolshagen G., McDonnell J. A. M., Mandeville J.-C., Kearsley A. T. and Ludwig H. (2005) Hypervelocity impacts on HST solar arrays and the debris population. *Advances in Space Research* **35**, 1243-1253.

Rietmeijer F. J. M. (1998) Interplanetary Dust Particles. In *Planetary Materials: Reviews in Mineralogy 36* (ed. J. J. Papike), Ch. 2, pp. 1-95. Mineralogical Society of America, Washington, D.C., USA.

See T. H., Mack K. S., Warren J. L., Zolensky M. E. and Zook H. A. (1994) Continued investigation of LDEF's structural frame and thermal blankets by the meteoroid and debris special investigation group. In: *LDEF- 69 months in space, NASA Conference publication 3194. Part 2* (ed. A. S. Levine), pp. 313-324. National Aeronautics and Space Administration, Washington, D.C., USA.

Tsou P., Brownlee D. E., Sandford S. A., Hörz F., Zolensky M. E. (2003) Wild-2 and interstellar sample collection and Earth return. *Journal of Geophysical Research (Planets)* **108(E10):** 8113, 10.1029/2003JE002109.

Tuzzolino A. J., Economou T. E., Clark B. C., Tsou P., Brownlee D. E., Green S. F., McDonnell J. A. M., and Colwell M. T. S. H. (2004) Dust Measurements in the Coma of Comet 81P/Wild2 by the Dust Flux Monitor Instrument. *Science* **304**, 1776 – 1780.

Wallis D., Solomon C. J., Kearsley A. T., Graham G. and McBride N. M. (2002) Modelling radially symmetric impact craters with Zernike Polynomials. *International Journal of Impact Engineering* **27. 4**, 433-457.

Warren J. L., Zook H. A., Allton J. H., Clanton U. S., Dardano C. B., Holder R. R. Marlow R. A., Schultz R. H., Watts L. A. and Wentworth S. J.(1989) The detection and observation of meteoroid and space debris impact features on the solar Max satellite. *Proceedings 19th Lunar and Planetary Science Conference*, 641-657.

Wooden D. H, Harker D. E., Woodward C. E., Butner H. M, Koike C., Witteborn F. C. and McMurtry C. W. (1999) Silicate mineralogy of the dust in the inner coma of comet C/1995 01 (Hale-Bopp) pre and post-perihelion. *Astrophysical Journal* **517**, 1034-1058.

Zolensky M. E., Zook H. A., Hörz F., Atkinson D. R., Coombs C. R., Watts A. J., Dardano C. B., See T., Simon C. G. and Konard W. H. (1994) Interim Report of the Meteoroid and Debris Special Investigation Group. In: *LDEF- 69 months in space, NASA Conference publication 3194. Part 2* (ed. A. S. Levine), pp. 277-302. National Aeronautics and Space Administration, Washington, D.C., USA.

Figure captions

Figure 1. The Stardust aerogel collector aluminium frame, with an enlarged detail of four foil sheets (reflective, appearing dark) around an aerogel block. Image courtesy of NASA/JPL-Caltech.

Figure 2. Montage of secondary electron images, showing numerous impacts by soda lime glass spheres, of 62 microns diameter.

Figure 3. Plot of SEM digital caliper measurements on Richardson test slide features (Y-axis) against certified values (X-axis). Note excellent linear correlation within 1% of certified values.

Figure 4. Backscattered electron image of a piece of the Stardust Al 1100 foil, showing linear surface striations, channelling contrast from discrete metal grains (variations in background grey-tone), and iron-rich alloy inclusions (bright areas).

Figure 5. Backscattered electron images of soda lime glass bead projectiles, showing uniform size in the nominal 22.8 micron sample (left), but broader distribution in the nominal 11.58 micron sample (right). Note digital measurement calipers on images.

Figure 6. Particle diameter histograms for the soda lime glass bead projectiles used for light gas gun shots at NASA and Kent.

Figure 7. A foil-wrapped 15mm plate, mounted upon an aluminium base-plate (drilled with four locating holes for support), is placed on the target holder in the light gas gun chamber at Kent.

Figure 8. Backscattered electron image of a vertical section through an impact crater on aluminium. Crater diameter is defined as length of the horizontal line indicated.

Figure 9. Comparison of secondary electron (left) and backscattered electron images (right) showing topographic contrast used to define horizontal surface of crater lip.

Figure 10. Secondary electron image of a crater produced by impact of a grain of the pyroxene enstatite on Stardust foil. The lines of three diameter measurements by digital callipers are shown.

Figure 11. Histograms of impact crater diameters for each wrapped foil shot at Kent.

Figure 12. Histograms of impact crater diameters for each wrapped foil shot at NASA.

Figure 13. Plots of average impact crater diameter against projectile average diameter: for all craters greater than four times the projectile average diameter (excepting the data point for the smallest projectiles).

Figure 14. Backscattered electron image of an impact crater on titanium metal (left), and projection of a three dimensional digital model derived from tilted inclination images of the same crater (right). It is possible to measure both crater depth below, and crater inner diameter at the ambient target surface. Reconstruction using MEX software, courtesy of Alicona Imaging GmbH.

Table 1: **Light Gas Gun shots with soda-lime sphere projectiles.**

Soda lime glass projectiles	**Nominal Projectile Diameter ± σ (microns)**	**Projectile Diameter Measured ± σ (microns) Sample [n]**	**Impact speed (km s^{-1}) ±2%**	**No. of craters on foil**	**All Crater Diameters SEM average ± σ (microns) [max/min avg and σ]**
Kent	11.58 ± 0.19	9.84 ± 2.23 [104]	5.93	51	39.41 ± 8.73 [1.07 ± 0.04]
NASA	11.58 ± 0.19	9.84 ± 2.23 [104]	6.06	44	51.04 ± 9.46 [1.05 ± 0.03]
Kent	22.81 ± 0.78	21.87 ± 0.92 [35]	5.97	62	81.75 ± 23.93 [1.05 ± 0.03]
Kent (free rear)	22.81 ± 0.7	21.87 ± 0.92 [35]	5.92	47 (part)	95.43 ± 10.28 [1.06 ± 0.04]
NASA	22.81 ± 0.78	21.87 ± 0.92 [35]	6.12	38	81.52 ± 27.3 [1.05 ± 0.03]
Kent	35.0 ± 0.8	34.72 ± 1.01 [94]	6.05	32	143.13 ± 26.35 [1.06 ± 0.04]
NASA	35.0 ± 0.8	34.72 ± 1.01 [94]	6.21	101	173.58 ± 38.94 [1.05 ± 0.03]
Kent	42.68 ± 0.55	42.3 ± 1.02 [25]	6.09	91	184.33 ± 26.43 [1.05 ± 0.03]
NASA	49.21 ± 0.72	49.29 ± 3.17 [118]	6.03	93	228.88 ± 30.78 [1.05 ± 0.03]
Kent	63.84 ± 0.8	64.05 ± 2.8 [75]	6.05	74	278.53 ± 30.44 [1.07 ± 0.04]
Kent	83.4 ± 0.8	84.18 ± 2.8 [49]	6.22	38	364.86 ± 45.49 [1.04 ± 0.02]
Kent (free rear)	83.4 ± 2.0	84.18 ± 2.8 [49]	5.96	8	385.71 ± 10.97 [1.03 ± 0.02]
Kent (empty sabot)	N/A	N/A	N/A	14	40.57 ± 16.38

Crater diameters are based upon the raw data set, with no threshold for fragmented projectiles. N/A (not applicable) refers to the empty sabot shot where there are no known appropriate dimensions for intended projectiles.